3.3.2.4 Stress Determination

The isochromatic phase is converted to the $\sigma_1 - \sigma_2$ fields using Equation (3.1). The two CGS phases are converted to stress derivatives using Equation (2.26) and then integrated using the PCG method, producing $\sigma_1 + \sigma_2 + c_i$, where c_i is a constant of integration. This constant may be determined by using one of the traction-free boundary conditions along the notch edge, $\sigma_{\theta\theta} = 0$ or $\sigma_{r\theta} = 0$ for $\theta = \pm 5\pi/6$, where θ denotes the rotational polar coordinate. Utilizing the $\sigma_1 - \sigma_2$, $\sigma_1 + \sigma_2 + c_i$, and α fields, shown in Figures 3.15(a)–3.15(c), the $\sigma_{\theta\theta} = 0$ condition gives a constant of integration calculated by

$$c_i = [(\sigma_1 + \sigma_2 + c_i) - (\sigma_1 - \sigma_2)\cos(2\alpha - 2\theta)]\big|_{\theta=\pm 5\pi/6}. \tag{3.13}$$

With this constant of integration, the $\sigma_1 + \sigma_2$ field is determined, as shown in Figure 3.15(d). The experimental field is asymmetric across the x axis, unlike the theoretical field in Figure 3.15(e), but this is due to an asymmetric x derivative of $\sigma_1 + \sigma_2$, just noticeable along the V-notch boundary in the experimental unwrapped horizontal shearing φ_{sum} in Figure 3.14(a). Otherwise, the stress concentration variation with r appears to generally agree with theory. With full-field $\sigma_1 + \sigma_2$ and $\sigma_1 - \sigma_2$, the principal stresses may be separated, as shown in Figure 3.16. The experimental principal stresses compare well with theory, with the σ_1 field with a single elliptical lobe symmetric about the x axis and the σ_2 field with a kidney bean shape again symmetric about the x axis. The experimental σ_1 is smaller in stress magnitude than the theoretical field, while the experimental σ_2 is larger in stress magnitude than the theoretical field; these differences are likely due to the experimental $\sigma_1 - \sigma_2$ field being slightly larger in stress magnitude than the theoretical data.

The Cartesian stresses, σ_{xx}, σ_{yy}, and σ_{xy}, shown in Figure 3.17, are determined using the separated principal stresses and the isoclinic angle as the angle of rotation for the coordinate transformation. These and the polar stresses may also be written in terms of $\sigma_1 - \sigma_2$, $\sigma_1 + \sigma_2$, α, and θ (for the polar stresses), as shown in Table 3.3 (derivation of these relationships and others concerning stresses may be found in Appendix A); these formulas indicate how the in-plane stresses relate to the fields from the two experimental methods. The experimental σ_{xx} field has the correct single elliptical lobe shape about the x axis as compared to the theoretical σ_{xx}. The kidney bean-shaped contour appears in both the experimental and theoretical σ_{yy}. The interpolated regions in the isoclinic angle visually appear to modulate the experimental σ_{xy} as compared to the theoretical σ_{xy}, but positive stresses for $(-x, +y)$ and $(+x, -y)$ regions and negative stresses for $(+x, +y)$ and $(-x, -y)$ regions are evident. The effect of α on this shear stress field is not surprising since σ_{xy} only depends on the photoelastic data, as seen in the formula in Table 3.3, and thus the error in α is not diffused by $\sigma_1 + \sigma_2$ for this field.

Stress	Relationship to $\sigma_1 - \sigma_2$, $\sigma_1 + \sigma_2$, α, and θ
σ_{xx}	$\frac{1}{2}(\sigma_1 + \sigma_2) + \frac{1}{2}(\sigma_1 - \sigma_2)cos(2\alpha)$
σ_{yy}	$\frac{1}{2}(\sigma_1 + \sigma_2) - \frac{1}{2}(\sigma_1 - \sigma_2)cos(2\alpha)$
σ_{xy}	$\frac{1}{2}(\sigma_1 - \sigma_2)sin(2\alpha)$
σ_{rr}	$\frac{1}{2}(\sigma_1 + \sigma_2) + \frac{1}{2}(\sigma_1 - \sigma_2)cos(2\theta - 2\alpha)$
$\sigma_{\theta\theta}$	$\frac{1}{2}(\sigma_1 + \sigma_2) - \frac{1}{2}(\sigma_1 - \sigma_2)cos(2\theta - 2\alpha)$
$\sigma_{r\theta}$	$-\frac{1}{2}(\sigma_1 - \sigma_2)sin(2\theta - 2\alpha)$

Table 3.3: In-plane stress components and their relationships to $\sigma_1 - \sigma_2$, $\sigma_1 + \sigma_2$, α, and θ

The polar stresses presented in Figure 3.18 are determined by transforming the Cartesian stresses with a rotation matrix with θ as the angle of rotation. Similar to the Cartesian stresses, the experimental polar stresses compare well with theoretical fields, with overall good shape comparison and stress magnitude comparison despite modulation by the errors in the isoclinic angle. The experimental σ_{rr} field is asymmetric about the x axis with larger stress magnitude for positive y values. The experimental $\sigma_{\theta\theta}$ has the wide fan-like structure in front of the notch, though not all of the $\sigma_{\theta\theta}$ data is going to zero along the notch mask boundary, requiring a choice of where to apply the boundary condition for the constant of integration calculation. The portion of the boundary that appears to be furthest in proximity from error sources like interpolated regions in α and far from the $\cos\varphi_{diff} \rightarrow 0$ boundaries is chosen for the constant of integration calculation. The experimental $\sigma_{r\theta}$ is noticeably modulated by the isoclinic angle errors, but the overall asymetric stresses match well with theoretical values, even better than the experimental σ_{xy} compares with theory. Since $\sigma_{r\theta}$ depends on both α and θ in that $\sigma_{r\theta} = \frac{1}{2}(\sigma_1 - \sigma_2)sin(2\theta - 2\alpha)$, the θ contributions appear to diffuse the error associated with α, allowing for better agreement with theory for $\sigma_{r\theta}$ than for σ_{xy}.

In general, the stress fields appear to match well in magnitude for larger r, but the largest difference between the theoretical and experimental stress fields is close to the notch tip. This greater difference near the notch tip is expected because the finite resolution of the experimental techniques and the $1/r^{1-\lambda_o}$ character of the stress fields make the large fringe density near the notch tip more difficult to measure. The slight asymmetry of the stress fields about the x axis, especially along the notch edge, is evidence that the polycarbonate specimen is not perfectly uniformly loaded. Another possible source of error in the data is due to the masking of the notch area, which obscures the exact edge of the notch where the boundary conditions are applied and, hence, where the constant of integration is calculated. The slightly higher stress concentration for $\sigma_1 - \sigma_2$ and slightly lower stress concentration for $\sigma_1 + \sigma_2$ in the experimental data, as compared to the theoretical data, is possibly due to the material constants used to convert the phases to stresses, given in Section 3.3.1. Polymers tend to vary between manufacturers and between different batches of material, leading to variable material properties. Since the material constants used are from published literature, these may not *exactly* correspond to the material properties of the polycarbonate used in this study. The constants in literature are good guidelines and a place to start for converting these phases to stresses. The combination of these constants from literature may lead to an under-determination of the stresses in $\sigma_1 + \sigma_2$, leading to a smaller choice of the fitting coefficient C_f, which is the reason for the theoretical $\sigma_1 - \sigma_2$ appearing too small. In future, to more accurately determine the stresses, these material constants can be measured for the particular batch of polymer used for the specimens.

Given all of these considerations, the data fit remarkably well. One measure of the global error is the root mean square deviation (RMSD) normalized by the range of data, denoted NRMSD. Only data points not masked by notch mask are considered here. Table 3.4 reports the error analysis of several fields. The fields with the lowest NRMSD are the stress derivatives and $\sigma_1 - \sigma_2$, demonstrating the effectiveness of the six-step phase-shifting photoelastic method and small effect of the $T_x \approx T_y$ assumption and the e_1 $\lambda/4$ plate misalignment error. Additionally, since the theoretical stress field fitting factor C_f is calculated by comparison with the all of the experimental fields, the low error for both the stress derivatives and $\sigma_1 - \sigma_2$ fields that come from two separate experimental techniques implies that these two techniques work well together to determine the full-field stress tensor.

The isoclinic angle has a higher NRMSD, though still reasonable at 7.5%, most likely due to the interpolation across the regions near $\sin(\delta) = 0$, since 27% of the data points (excluding the masked notch region) have been removed and interpolated across. Importantly, without this interpolation, the isoclinic angle from this photoelastic data cannot be unwrapped properly with the presence of many false discontinuities due to a nonzero tolerance in $(T_x - T_y)$ and the e_1 $\lambda/4$ plate misalignment error. The interpolation method is a necessary step that makes the isoclinic angle into usable data to combine with the stress fields, making the error introduced by the interpolated regions tolerable. An error source in the stress fields employing the $\sigma_1 + \sigma_2$ field is the constant of integration calculation, which is, first, dependent of the isoclinic angle, and, second, taken not precisely at $\theta = \pm 5\pi/6$. Since the notched area requires a mask to prevent corruption of the data near the edges during phase unwrapping, then $\theta = \pm 5\pi/6$ is obscured. Here, c_i comes from $\theta = -2.54\ rad. = -145^o$. Despite these considerations, the experimental full-field stresses in principal, Cartesian, and polar coordinate systems have acceptable NRMSD error, ranging from 3.3% to 9.7%, demonstrating that the combined CGS-photoelasticity phase-shifting method successfully determines the in-plane tensorial stress for photoelastic materials.

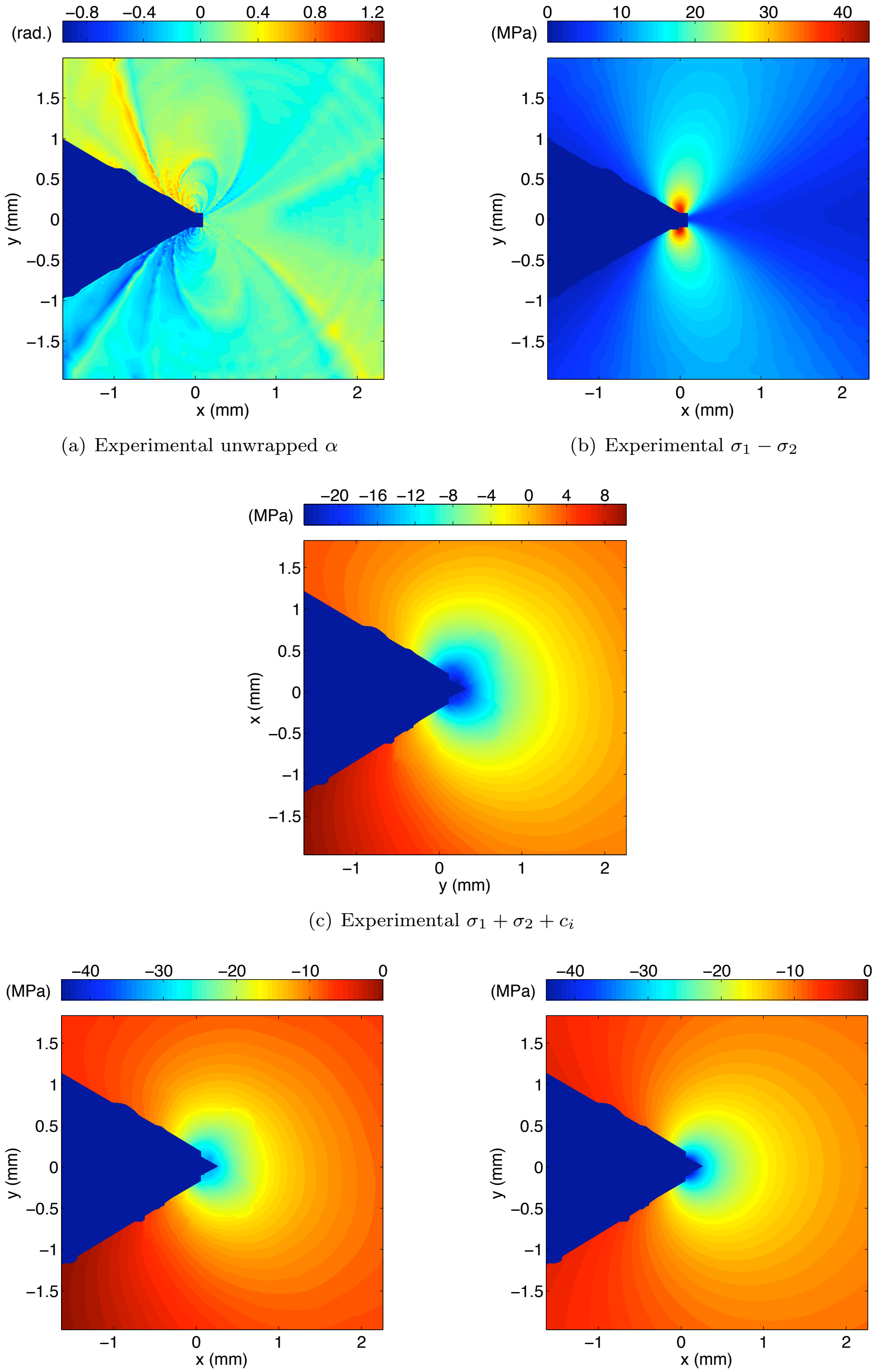

(a) Experimental unwrapped α

(b) Experimental $\sigma_1 - \sigma_2$

(c) Experimental $\sigma_1 + \sigma_2 + c_i$

(d) Experimental $\sigma_1 + \sigma_2$

(e) Theoretical $\sigma_1 + \sigma_2$

Figure 3.15: Combined principal stress fields for the compressed polycarbonate V-notch plate with V-notch masks in blue

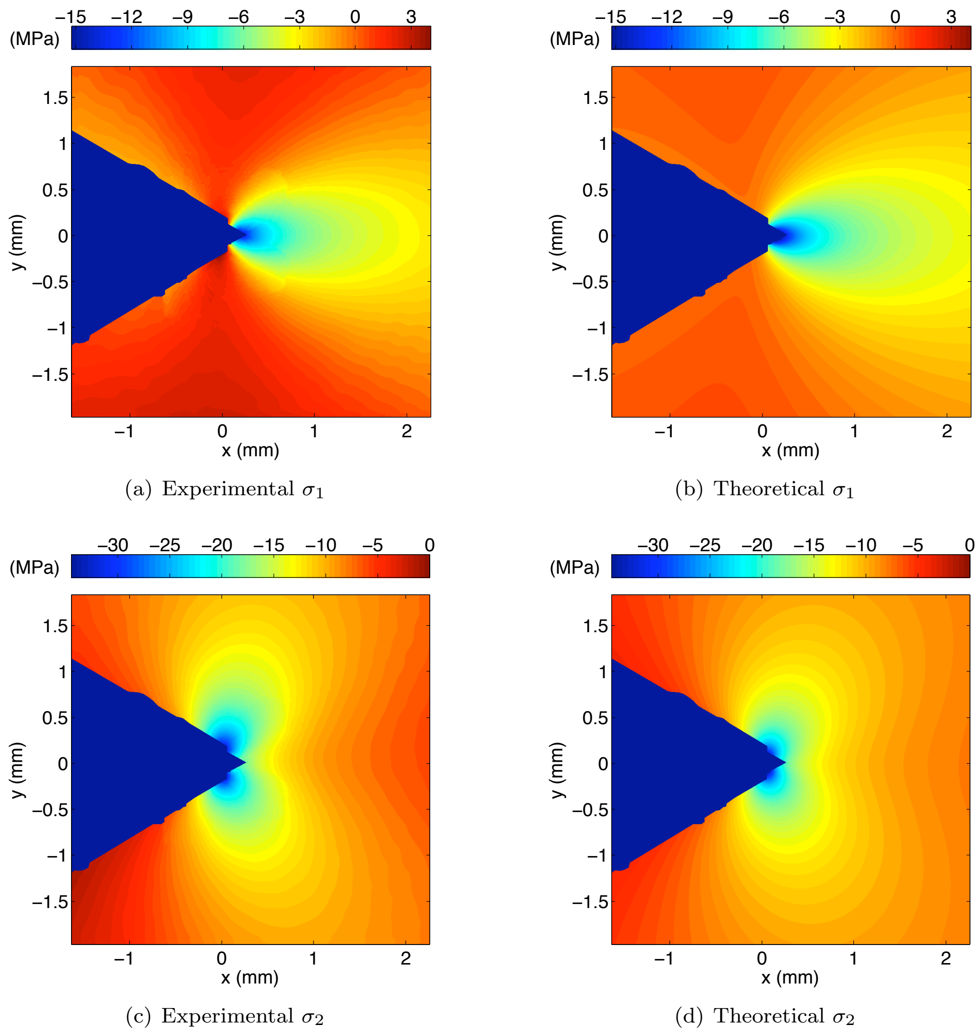

(a) Experimental σ_1

(b) Theoretical σ_1

(c) Experimental σ_2

(d) Theoretical σ_2

Figure 3.16: Experimental and theoretical separated principal stress fields for the compressed polycarbonate V-notch plate with V-notch masks in blue

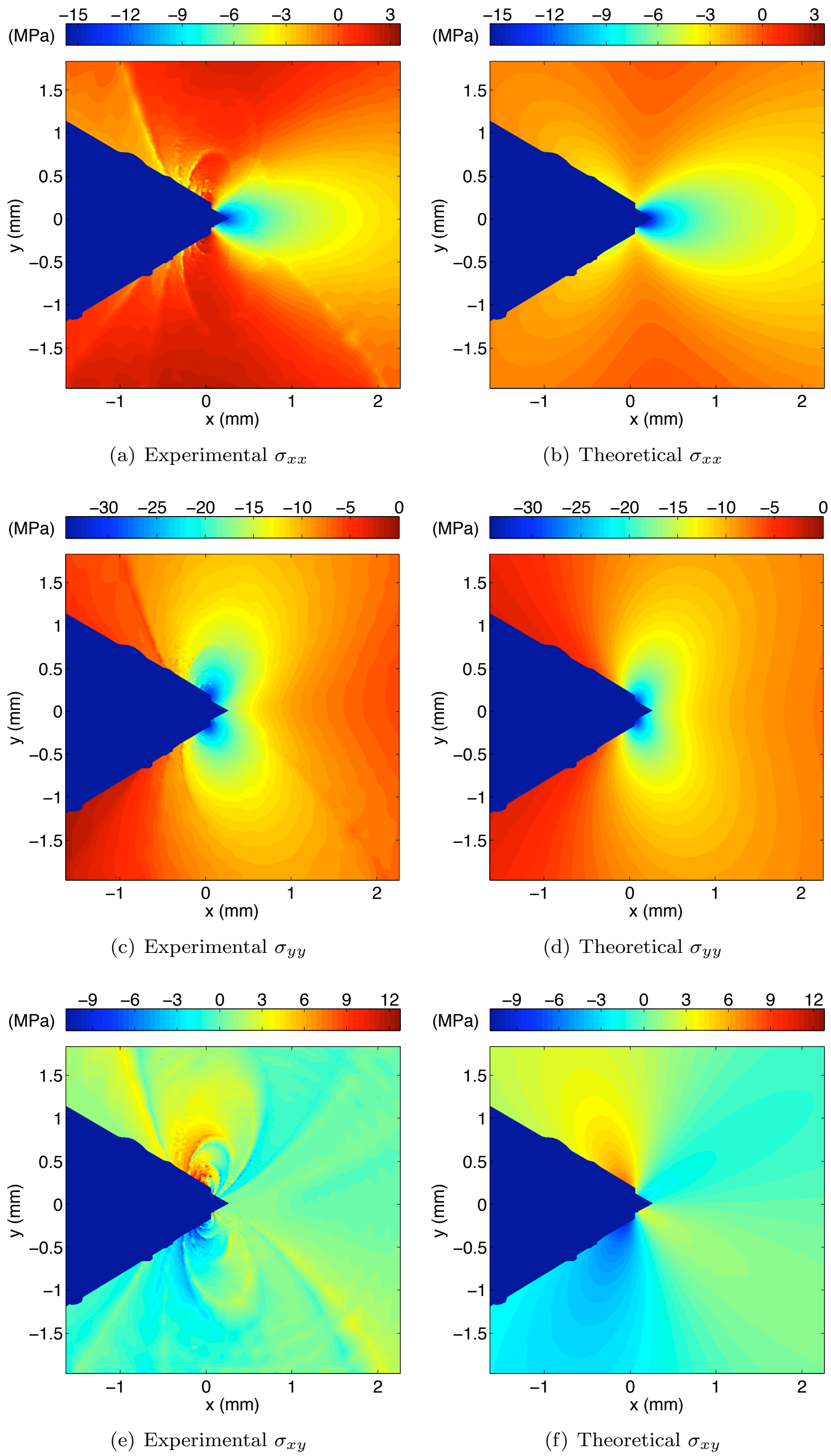

Figure 3.17: Experimental and theoretical Cartesian stress fields for the compressed polycarbonate V-notch plate with V-notch masks in blue

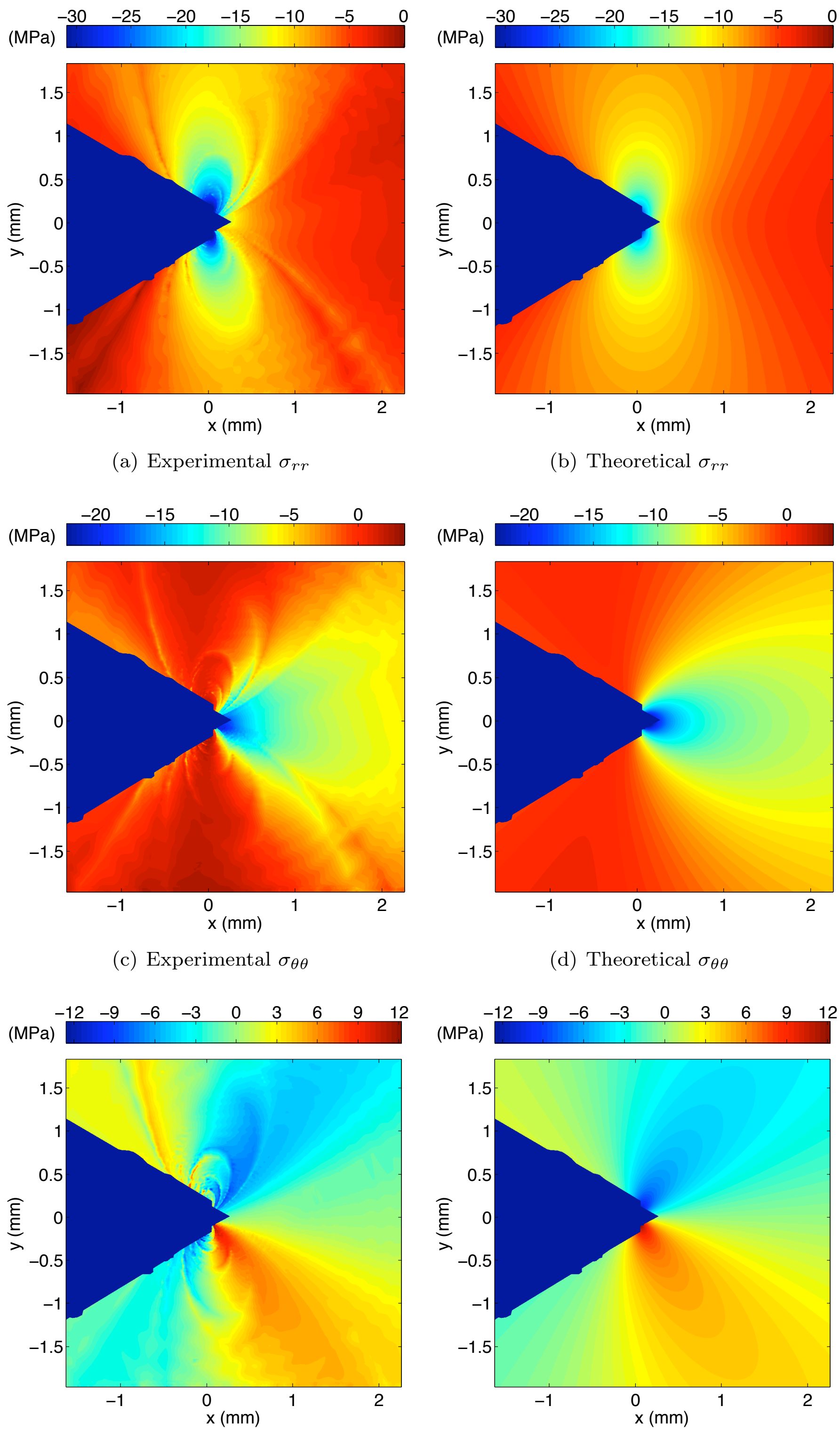

Figure 3.18: Experimental and theoretical polar stress fields for the compressed polycarbonate V-notch plate with V-notch masks in blue

Quantity	Units	RMSD (in Units)	Data Range (in Units)	NRMSD (No Units)
α	rad.	0.17	2.25	0.075
$\partial(\sigma_1 + \sigma_2)/\partial x$	MPa/mm	1.55	94.2	0.016
$\partial(\sigma_1 + \sigma_2)/\partial y$	MPa/mm	1.31	110.0	0.012
$\sigma_1 + \sigma_2$	MPa	1.52	33.7	0.045
$\sigma_1 - \sigma_2$	MPa	1.62	42.1	0.038
σ_1	MPa	1.28	17.3	0.074
σ_2	MPa	0.99	30.1	0.033
σ_{xx}	MPa	1.62	16.9	0.097
σ_{yy}	MPa	1.17	29.8	0.039
σ_{xy}	MPa	1.95	23.7	0.040
σ_{rr}	MPa	1.14	13.4	0.085
$\sigma_{\theta\theta}$	MPa	1.41	34.6	0.041
$\sigma_{r\theta}$	MPa	1.26	23.1	0.055

Table 3.4: Error analysis for various experimental fields for the compressed polycarbonate V-notch plate

3.4 Conclusions

The combined phase-shifting photoelasticity and CGS method presented in this study demonstrates the full-field determination of the in-plane tensorial stress for photoelastic materials. A six-step phase-shifting photoelasticity method gives $\sigma_1 - \sigma_2$ and the isoclinic angle, which requires some careful consideration in regions where $\sin(\delta) \rightarrow 0$ to minimize errors in phase unwrapping. Transmission CGS for a photoelastic material requires a four-step phase-shifting method in conjunction with polarization optics prior to the specimen to extract the desired phases related to x and y derivatives of $\sigma_1 + \sigma_2$. A weighted PCG algorithm is used for both phase unwrapping and integration of the $\sigma_1 + \sigma_2$ derivatives. The $\sigma_1 + \sigma_2$ field is determined by using a boundary condition to determine the constant of integration. The principal stresses are then separable from the $\sigma_1 + \sigma_2$ and $\sigma_1 - \sigma_2$ fields. The Cartesian and polar coordinate stress fields are also determined by simple coordinate transformations using the isoclinic angle and the polar coordinate. The entire method is demonstrated for a compressed polycarbonate plate with a side V-notch.

Possible error sources in the experimental method are identified as the transmission and reflectance coefficients of the non-polarizing beamsplitter and rotational misalignment of the polarization optics. Theoretical data including these possible errors demonstrate the extent of their effect on the data and identify the dominant error source in the experimental data as the misalignment of the first $\lambda/4$ plate. Mitigation techniques, such as correction of the modulated wrapped isoclinic angle and implementation of the PCG algorithm, a data quality-driven unwrapping algorithm, help to minimize propagation of error through the data. Despite these errors, the experimental stresses compare well with the theoretical stresses for the polycarbonate example. Establishing the use of this hybrid experimental technique in a compressed plate with a V-notch is the foundation for its application to determine the in-plane tensorial stress around a loaded crack in a photoelastic material.